JOURNAL OF COMPUTATIONAL PHYSICS 81, 444–480 (1989)

A Reduced Gravity, Primitive Equation Model of the Upper Equatorial Ocean

PETER R. GENT

National Center for Atmospheric Research, P.O. Box 3000, Boulder, Colorado 80307

AND

MARK A. CANE

Lamont–Doherty Geological Observatory, Palisades, New York 10964

Received December 3, 1987; revised May 5, 1988

This paper describes a fourth-order finite difference model of the equatorial ocean that is designed to study dynamic and thermodynamic processes on time scales of a decade or less. It is a primitive equation model employing the reduced gravity assumption so that the deep ocean is at rest below the active upper ocean. The model consists of a surface mixed layer and an active layer below, which is divided into an arbitrary number of numerical layers by means of a sigma coordinate. The model can be used in an unstratified version, when temperature acts as a passive tracer, as well as in the full stratified version. The numerical formulation of the model is described in detail. Experiments comparing three different horizontal smoothers: Shapiro filter, Laplacian friction, and biharmonic friction are presented. It is concluded that, at the level needed to maintain computational stability, the Shapiro filter damps the fields least; in addition, it is faster and easier to implement when the horizontal finite difference grid is stretched.

1. INTRODUCTION

The El Niño–southern oscillation phenomenon is the largest interannual signal in the earth's climate. Extensive observations of this phenomenon are, and will be, taken during the ten year Tropical Ocean–Global Atmosphere (TOGA) program. One of TOGA's scientific objectives is to explore the potential of coupled atmosphere ocean models for predicting climate variability. In this paper we describe a numerical model of the equatorial ocean that is specifically designed for TOGA studies. Thus there is particular emphasis on thermodynamic processes because sea surface temperature is the most important ocean variable to the atmosphere. The model domain can also be limited both in the horizontal and vertical, and thus this primitive equation model uses the reduced gravity assumption so that the deep ocean is at rest below the active upper ocean. This assumes that only the

0021-9991/89 $3.00

near equatorial upper ocean is important for the dynamic and thermodynamic processes of the TOGA problem on the annual time scale, which means that model integration times should be no longer than several years.

The numerical model consists of a surface mixed layer and an active layer below, which is divided into an arbitrary number of numerical layers by means of a sigma coordinate. This means that the vertical resolution is fine exactly where it is needed below the mixed layer, where there are very large shears in both velocity and temperature in the equatorial oceans. This overcomes a disadvantage of level models which need fine resolution over a greater vertical extent when the depth of the well-mixed layer varies considerably. In the Pacific ocean this depth varies from less than 20 m in the east to about 75 m in the west. This model predicts the depth of this layer, and then concentrates its resolution below much more efficiently than does a level model. The horizontal domain is a rectangular equatorial β-plane, and the model can employ a stretched grid. This gives enhanced resolution at the equator and model boundaries in order to resolve better the smaller scale phenomena that occur in these locations. In most of the experiments described in this paper, however, the mixed layer has a constant depth and the horizontal grid is uniform.

Observations and theory of the equatorial oceans suggest that the dominant sinks of energy and heat are vertical friction and vertical diffusion, see [8, 10], for example. The model was designed to mimic this situation. Momentum and heat are input as body forces in the upper mixed layer, are diffused downwards quite strongly, and are lost to the resting, constant temperature deep ocean. The vertical coefficients are based on observations and are larger than those normally used in midlatitude ocean models. As a horizontal "eddy viscosity" we chose to use the Shapiro filter [12] with the intent of suppressing nonlinear computational instability while keeping the horizontal sinks of energy and heat much smaller than the vertical sinks. Results presented in this paper show that this is indeed the case. We also compare experiments using the filter with those using the more familiar horizontal smoothing techniques of Laplacian and biharmonic friction and show that the horizontal sinks due to these frictional forms are larger than those due to the Shapiro filter. These comparisons are made in experiments that spin up from rest to an equilibrium state and also in spindown experiments over a period of 100 days.

This numerical model was developed from a two-layer, unstratified model that is described in [2, 3]. The present model can also be used in an unstratified version when the temperature acts as a passive tracer. The first comparison experiments described below use this version of the model, while the second comparison experiments use the full stratified version with five layers. Both versions use the same time integration method as the original model, which is the N-cycle scheme of Lorenz [7].

The plan of the paper is as follows. The model continuous equations are given in Section 2, while the finite difference equations are given in Section 3. The vertical coordinate, forcing, and vertical mixing are described in Section 4, the horizontal

smoothing and friction in Section 5, and the time method and its stability in Section 6. The unstratified and stratified model experiments are presented in Sections 7 and 8, and the reasons for our choice of the filter are discussed in Section 9. Our conclusions are listed in Section 10.

2. Continuous Equations

(a) *Generalized Cartesian Coordinate*

This derivation follows that in [11] with the extension of including a free surface elevation z_T. It uses a generalized vertical coordinate, $s(x, y, z, t)$, so we define

$$h(x, y, s, t) = \frac{\partial z}{\partial s} \tag{1}$$

and

$$w_e = h\frac{Ds}{Dt} = w - \frac{\partial z}{\partial t} - \mathbf{u}\cdot\nabla z. \tag{2}$$

h is then the height between, and w_e the volume flux per unit area across, surfaces of constant s. $\mathbf{u}$ and ∇ are the 2-dimensional horizontal velocity and gradient operator, respectively. The incompressible, hydrostatic equations of motion in these generalized cartesian coordinates can be found in [5] and are

$$\frac{D\mathbf{u}}{Dt} + f\mathbf{k}\times\mathbf{u} + \frac{1}{\rho}\nabla p + g\nabla z = \frac{1}{h}\frac{\partial \boldsymbol{\tau}}{\partial s} + \mathbf{F}, \tag{3}$$

$$\frac{D\rho}{Dt} = \frac{1}{h}\frac{\partial Q'}{\partial s} + D', \tag{4}$$

$$\frac{1}{h}\frac{Dh}{Dt} + \nabla\cdot\mathbf{u} + \frac{\partial}{\partial s}\left(\frac{w_e}{h}\right) = 0, \tag{5}$$

$$\frac{\partial p}{\partial s} + \rho g h = 0. \tag{6}$$

Here $\mathbf{k}$ is the unit vertical vector, p is pressure, ρ is density, and g is gravity. Also

$$\frac{D}{Dt} = \frac{\partial}{\partial t} + \mathbf{u}\cdot\nabla + \frac{w_e}{h}\frac{\partial}{\partial s}, \tag{7}$$

all gradient operations are with respect to constant s, $\boldsymbol{\tau}$ is stress, Q' is the density flux, and $\mathbf{F}$ and D' are horizontal friction and density damping.

(b) *Boussinesq Approximation*

We define the buoyancy b and a modified pressure P such that

$$b \equiv -g\left(\frac{\rho-\rho_0}{\rho_0}\right), \tag{8}$$

$$\frac{\partial P}{\partial s} \equiv bh, \tag{9}$$

where ρ_0 is a constant reference density. The hydrostatic equation (6) then becomes

$$\frac{1}{\rho_0}\frac{\partial p}{\partial s} + g\frac{\partial z}{\partial s} - \frac{\partial P}{\partial s} = 0. \tag{10}$$

Integrating this equation with the boundary condition $p=0$ at $s=s_T$ gives

$$\frac{p}{\rho_0} = P - P_T - g(z-z_T), \tag{11}$$

which simplifies by taking

$$P_T = gz_T; \tag{12}$$

i.e., the modified pressure at the surface equals g times the free surface elevation. The momentum equation (3) can now be written in the form

$$\frac{\rho}{\rho_0}\left(\frac{D\mathbf{u}}{Dt} + f\mathbf{k}\times\mathbf{u}\right) + \nabla P - b\nabla z = \frac{\rho}{\rho_0}\left(\frac{1}{h}\frac{\partial \boldsymbol{\tau}}{\partial s} + \mathbf{F}\right). \tag{13}$$

The Boussinesq approximation in s coordinates is then to set ρ/ρ_0 equal to one in Eq. (13) which becomes

$$\frac{D\mathbf{u}}{Dt} + f\mathbf{k}\times\mathbf{u} + \nabla P - b\nabla z = \frac{1}{h}\frac{\partial \boldsymbol{\tau}}{\partial s} + \mathbf{F}. \tag{14}$$

In general the buoyancy is a function of temperature and salinity. For the present, however, we ignore the effects of salinity and further simplify the equations by assuming that b is only a linear function of T, i.e.,

$$b = b(T) = \alpha g(T - T_B), \tag{15}$$

where T_B is a constant reference temperature and α is the coefficient of thermal expansion. Substituting from Eqs. (8) and (15) into the density equation (4) gives an equation for temperature; namely,

$$\frac{DT}{Dt} = \frac{1}{h}\frac{\partial Q}{\partial s} + D. \tag{16}$$

Here Q is the downward heat flux divided by $\rho_0 c_p$, where c_p is the specific heat of water at constant pressure, and D is the thermal damping.

(c) *Reduced Gravity Approximation*

The reduced gravity approximation is to assume that below a certain depth the ocean is at rest and has a constant density, or in this model a constant temperature. In s coordinates the no-flow assumption requires no pressure force at the base of the model $s = s_B$, i.e.,

$$\nabla P - b\nabla z = 0 \qquad \text{at} \quad s = s_B. \tag{17}$$

This can be satisfied by choosing

$$b_B = 0, \qquad P_B = 0 \qquad \text{at} \quad s = s_B, \tag{18}$$

which is accomplished by setting the temperature of the deep ocean to T_B (i.e., zero buoyancy in the deep ocean, see (15)) and (from integrating Eq. (9)) setting

$$P_T = \int_{s_B}^{s_T} bh \, ds. \tag{19}$$

Finally (14), (16), and (5) can be rewritten in flux form, viz.,

$$\frac{\partial}{\partial t}(h\mathbf{u}) + \nabla \cdot (\mathbf{u}h\mathbf{u}) + \frac{\partial}{\partial s}(w_e\mathbf{u}) + f\mathbf{k} \times h\mathbf{u} + h(\nabla P - b\nabla z) = \frac{\partial \boldsymbol{\tau}}{\partial s} + h\mathbf{F}, \tag{20}$$

$$\frac{\partial}{\partial t}(hT) + \nabla \cdot (\mathbf{u}hT) + \frac{\partial}{\partial s}(w_e T) = \frac{\partial Q}{\partial s} + hD, \tag{21}$$

$$\frac{\partial h}{\partial t} + \nabla \cdot (h\mathbf{u}) + \frac{\partial w_e}{\partial s} = 0. \tag{22}$$

The equations of the reduced-gravity, primitive equation model in s coordinates are (20) through (22), with z, P, and b defined by Eqs. (1), (9), and (15), respectively, and surface values of z and P given by Eqs. (12) and (19).

(d) *Boundary Conditions*

The inviscid boundary conditions are no normal flow at horizontal boundaries and no vertical flow at the top and bottom, i.e.,

$$\begin{aligned} \mathbf{u} \cdot \mathbf{n} &= 0 \qquad \text{on} \quad \delta\Omega, \\ w_e &= 0 \qquad \text{at} \quad s = s_T, s_B. \end{aligned} \tag{23}$$

The latter condition results from the assumption that the ocean surface and the base of the model are material surfaces. The viscous boundary conditions depend upon the form of the nonconservative forces $\mathbf{F}$ and D, but are either no-slip or free-slip and either zero heat flux or specified temperatures at horizontal boundaries.

(e) *Energy Equation*

The energy equation is formed by taking $\mathbf{u}\cdot(\mathbf{20})-\alpha gz(21)+(P+\alpha gzT_B)$ (22); it can then be manipulated into

$$\frac{\partial \varepsilon}{\partial t}+\nabla\cdot[\mathbf{u}(\varepsilon+hP)]+\frac{\partial}{\partial s}\left[\omega_e\left(\frac{\varepsilon}{h}+P\right)+P\frac{\partial z}{\partial t}\right]$$
$$=\mathbf{u}\cdot\left(\frac{\partial \boldsymbol{\tau}}{\partial s}+h\mathbf{F}\right)-\alpha gz\left(\frac{\partial Q}{\partial s}+hD\right), \tag{24}$$

where

$$\varepsilon=h(\tfrac{1}{2}\mathbf{u}\cdot\mathbf{u}-bz). \tag{25}$$

Integration of (24) over the total volume and use of boundary conditions (18), (19), and (23) show that the model energies are

$$\text{Kinetic Energy}=\iint_{\Omega} dx\,dy\int_{s_B}^{s_T}\tfrac{1}{2}h\mathbf{u}\cdot\mathbf{u}\,ds, \tag{26}$$

$$\text{Potential Energy}=\iint_{\Omega} dx\,dy\left[\int_{s_B}^{s_T}-hbz\,ds+\tfrac{1}{2}gz_T^2\right], \tag{27}$$

$$=\iint_{\Omega} dx\,dy\left[\int_{s_B}^{s_T}hb(z_T-z)\,ds-\tfrac{1}{2}gz_T^2\right]. \tag{28}$$

Thus the sum of kinetic and potential energy is conserved in inviscid, adiabatic flow. The potential energy has been defined such that it is zero if the buoyancy is zero ($T=T_B$) everywhere in the domain. This is an appropriate reference level for potential energy as it is the state the ocean will spin down to in the presence of vertical temperature diffusion. Manipulations of (21) and (22) and integrations over the total volume show that heat content and temperature variance are also conserved in inviscid, adiabatic flow, where

$$\text{Heat Content}=\iint_{\Omega} dx\,dy\int_{s_B}^{s_T}hb\,ds, \tag{29}$$

$$\text{Temperature Variance}=\iint_{\Omega} dx\,dy\int_{s_B}^{s_T}hb^2\,ds. \tag{30}$$

Again these quantities are zero if $T=T_B$ everywhere.

(f) *Unstratified Model*

An unstratified version of the model can be deduced from the stratified version if T and hence b and ρ, are kept constant throughout the model domain. In this case the constant b is called the reduced gravity (often denoted by g'), and Eq. (21)

for T is trivially satisfied or can be thought of as an equation for a passive scalar quantity. It is then easy to show that

$$P_T = gz_T = bH, \qquad \nabla P - b\nabla z = \frac{b\rho}{\rho_0}\nabla H, \tag{31}$$

where $H(x, y, t)$ is the total depth of the active ocean layer. The last equation in (31) gives the unstratified form of the pressure gradient force for use in (20). Equations (27) or (28) and (29) or (30) then give the unstratified potential energy and the conservation of the total fluid volume, i.e.,

$$\begin{aligned} \text{Potential Energy} &= \iint_\Omega dx\, dy\, \frac{1}{2}\frac{b\rho}{\rho_0} H^2, \\ \text{Constant} &= \iint_\Omega dx\, dy\, H. \end{aligned} \tag{32}$$

The boundary conditions are still those of Eq. (23).

(g) *Linearized Model*

A consistent linearization of the reduced-gravity primitive equation model in s-coordinates can be made and is given below. However, it is somewhat unfamiliar compared to the linearization in z-coordinates. One way to see this is that the hydrostatic equation in s-coordinates, (9), is nonlinear and is thus approximated in the linearization, whereas the equation is linear in z-coordinates and is thus retained exactly in the z-coordinate linearization. This results in an unfamiliar potential energy in the linearized s-coordinate model. For the linearized model the depth and buoyancy are divided into mean and fluctuating components as

$$\begin{aligned} h &= \bar{h}(s) + h', \\ b &= \bar{b}(s) + b'. \end{aligned} \tag{33}$$

The hydrostatic equation (9) and reduced gravity assumption (19) linearize to

$$\begin{aligned} \frac{\partial P}{\partial s} &= \bar{b}h + \bar{h}b', \\ P_T &\equiv gz_T = \int_{s_B}^{s_T} (\bar{b}h + \bar{h}b')\, ds. \end{aligned} \tag{34}$$

The momentum, heat, and continuity equations (20)–(22) linearize to

$$\frac{\partial}{\partial t}(\bar{h}\mathbf{u}) + f\mathbf{k}\times\bar{h}\mathbf{u} + \bar{h}(\nabla P - \bar{b}\nabla z) = \frac{\partial \boldsymbol{\tau}}{\partial s} + \bar{h}\mathbf{F}, \tag{35}$$

$$\frac{\partial}{\partial t}(h\bar{b} + \bar{h}b') + \nabla\cdot(\bar{h}\bar{b}\mathbf{u}) + \frac{\partial}{\partial s}(w_e\bar{b}) = \alpha g\left(\frac{\partial Q}{\partial s} + \bar{h}D\right), \tag{36}$$

$$\frac{\partial h}{\partial t} + \nabla\cdot(\bar{h}\mathbf{u}) + \frac{\partial w_e}{\partial s} = 0, \tag{37}$$

where (36) has been formulated in terms of buoyancy rather than temperature. The other model equations (1) and (15) remain unchanged. An energy equation for this model can be formed in exactly the same way as for the nonlinear version; the result is

$$\frac{\partial \varepsilon'}{\partial t} + \nabla \cdot [\mathbf{u}\bar{h}(P - \bar{b}z)] + \frac{\partial}{\partial s}\left[w_e(P - \bar{b}z) + P\frac{\partial z}{\partial t}\right]$$
$$= \mathbf{u} \cdot \left(\frac{\partial \tau}{\partial s} + \bar{h}\mathbf{F}\right) - \alpha g z \left(\frac{\partial Q}{\partial s} + \bar{h}D\right), \tag{38}$$

where

$$\varepsilon' = \frac{1}{2}\bar{h}\mathbf{u} \cdot \mathbf{u} + \frac{1}{2}\frac{(\bar{h}b')^2}{\partial \bar{b}/\partial s} - z(\bar{b}h + \bar{h}b').$$

Integration of (38) over the total volume shows that the linearized model energies are

$$\text{Kinetic Energy} = \iint_{\Omega} dx\, dy \int_{s_B}^{sT} \tfrac{1}{2}\bar{h}\mathbf{u} \cdot \mathbf{u}\, ds, \tag{39}$$

$$\text{Potential Energy} = \iint_{\Omega} dx\, dy \left[\int_{s_B}^{sT} \left[\frac{(1/2)(\bar{h}b')^2}{\partial \bar{b}/\partial s} - z(\bar{b}h + \bar{h}b') \right] ds + \frac{1}{2} g z_T^2 \right]. \tag{40}$$

A linearized version of the unstratified model can be found from the above equations by setting $\bar{b}$ to a constant and b' to zero in (33)–(37), which results in a kinetic energy given by (39) and a potential energy given by (32). The boundary conditions are unchanged in these linearized models.

(h) *Spherical Coordinates*

The model can also be defined in spherical rather than cartesian coordinates in which case $s = s(\lambda, \theta, z, t)$, where λ is longitude and θ latitude. In this case f in the momentum equation should be replaced by $f + u \tan \theta / R$, where R is the earth's radius, and the divergence operator has an extra geometric term, see [11].

3. Finite Difference Equations

(a) *Grid Configuration*

A stretched horizontal grid mesh is used to allow for increased resolution at the equator and lateral boundaries where phenomena with small spatial scales occur. The stretching is accomplished by solving an equation of the form

$$x_i^* = a + bx_i + \sum_j \alpha_j \tan^{-1}[\beta_j^{-1}(x_i - \gamma_j)], \tag{41}$$

for the location x_i of the ith point in physical space given that the points in computational space are equally spaced. Thus (41) is solved for the x_i that gives $x_i^* = (i-1)\,\Delta x$. In (41) β_j is a measure of the thickness of the stretched region at $x = \gamma_j$

and α_j is a weighting factor that determines how many mesh points will be in this stretched region. The stretching can be done at all four lateral boundaries and symmetrically about the equator, or can be ignored, giving a uniform grid in both computational and physical space. Horizontal cross sections of model variables can be plotted in either computational or physical space. This configuration and other details of finite differencing were first used in [2].

The vertical grid is shown in Fig. 1. We define

$$s_T = 0, \qquad s_B = -NZ, \qquad K = \tfrac{1}{2} - s, \tag{42}$$

where NZ is the number of model layers and K is an integer from one to NZ designating the midpoints of those layers. K is the opposite of s in that the layer numbers increase downwards in the model so that layer 1 is at the top and layer NZ at the bottom of the model, and the layer midpoints are designated by half integer values in the vertical coordinate s.

(b) *Horizontal Differencing*

In the horizontal all model variables are at the same locations at the corners of the grid squares (Scheme A in Arakawa's nomenclature). Single horizontal derivatives are calculated as

$$\frac{\partial f}{\partial x} = \frac{dx^*}{dx}\frac{\partial f}{\partial x^*} \approx \frac{dx^*}{dx}\delta f, \tag{43}$$

where dx^*/dx is calculated analytically from Eq. (41). In the interior δf is the fourth-order centered difference approximation defined by

$$\begin{aligned}\delta f_i &= \frac{1}{12\,\Delta x}\left[f_{i-2} - 8f_{i-1} + 8f_{i+1} - f_{i+2}\right], \\ &= \frac{\partial f}{\partial x^*}(x_j) - \frac{(\Delta x)^4}{30}\frac{\partial^5 f}{\partial x^{*5}}(x_j) + O(\Delta x)^6.\end{aligned} \tag{44}$$

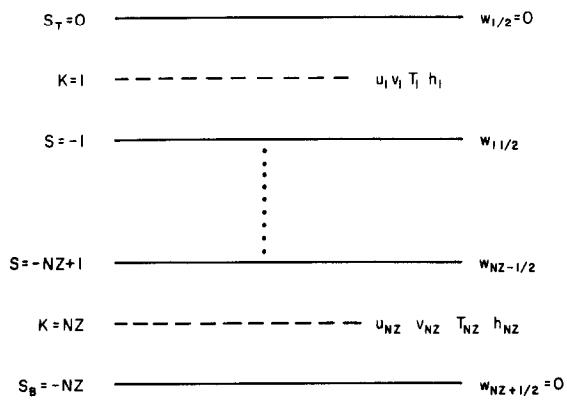

FIG. 1. The vertical finite difference grid.

At points on and next to the boundary, one-sided differences are used that are third-order accurate in Δx, but these are regions of finer resolution when the grid is stretched. The boundary forms are

$$\begin{aligned}\delta f_0 &= \frac{1}{6\,\Delta x}\,[-11 f_0 + 18 f_1 - 9 f_2 + 2 f_3], \\ &= \frac{\partial f}{\partial x^*}(x_0) + \frac{(\Delta x)^3}{4}\frac{\partial^4 f}{\partial x^{*4}}(x_0) + O(\Delta x)^4, \end{aligned} \tag{45}$$

$$\begin{aligned}\delta f_1 &= \frac{1}{6\,\Delta x}\,[-2 f_0 - 3 f_1 + 6 f_2 - f_3], \\ &= \frac{\partial f}{\partial x^*}(x_1) - \frac{(\Delta x)^3}{12}\frac{\partial^4 f}{\partial x^{*4}}(x_1) + O(\Delta x)^4. \end{aligned} \tag{46}$$

These boundary forms mean that continuous equations in conservation form will not be exactly conservative in finite difference form. This nonconservation will be discussed again later. The third-order boundary forms were necessary, however, because the fourth-order forms that were tried proved to be computationally unstable.

(c) *Vertical Differencing*

All model variables except w_e are held at layer midpoints, i.e., integer values of K, whereas w_e is held at the layer interfaces, i.e. integer values of s. Single vertical derivatives are simply calculated as

$$\begin{aligned}\delta f_K &= f_{K-1/2} - f_{K+1/2} \\ &= \frac{\partial f}{\partial s}(s_K) + \frac{(\Delta s)^2}{24}\frac{\partial^3 f}{\partial s^3}(s_K) + O(\Delta s)^4, \end{aligned} \tag{47}$$

since $\Delta s = 1$ across each layer. This form is second-order accurate in Δs. The flux form of the equations requires values of $\mathbf{u}$ and T at the layer interfaces, and we have chosen the forms

$$\mathbf{u}_{K+1/2} = \tfrac{1}{2}(\mathbf{u}_K + \mathbf{u}_{K+1}) \tag{48}$$

$$T_{K+1/2} = \frac{(h_K T_K + h_{K+1} T_{K+1})}{(h_K + h_{K+1})}. \tag{49}$$

These forms conserve total energy and heat content in finite difference form but not temperature variance unless the layer depths h_K are equal (see below).

(d) *Pressure Gradient Force*

In this subsection the finite difference form of some of the model equations and the form of the pressure gradient force will be given. Equations (1), (9), (15), and (19) are represented by finite difference forms in the following obvious way

$$z_K - z_T = -\left(\sum_{j=1}^{K-1} h_j + \frac{h_K}{2}\right), \tag{50}$$

$$P_K - P_T = -\left(\sum_{j=1}^{K-1} h_j b_j + \frac{h_K b_K}{2}\right), \tag{51}$$

$$b_K = \alpha g (T_K - T_B), \tag{52}$$

$$P_T = g z_T = \sum_{K=1}^{NZ} h_K b_K. \tag{53}$$

These finite difference forms are all centered approximations to the continuous forms. The finite difference form of the pressure gradient term in (20) is

$$\mathbf{PGF}_K = h_K (\nabla P_K - b_K \nabla z_K), \tag{54}$$

where the gradient operator now means the finite difference form given by (43)–(46). After manipulation using (50)–(53), this can be written in the form

$$\mathbf{PGF}_K = h_K \left\{ (g - b_K) \nabla z_T + b_K \nabla \left[\sum_{j=1}^{K-1} h_j + \frac{h_K}{2} \right] - \nabla \left[\sum_{j=1}^{K-1} h_j b_j + \frac{h_K b_K}{2} \right] \right\}, \tag{55}$$

where the free surface elevation z_T is given by (53) and is calculated diagnostically in the model.

(e) *Model Equations*

The finite difference form of the continuity equation (22) is the obvious form

$$\frac{\partial h_K}{\partial t} + \nabla \cdot (h_K \mathbf{u}_K) + w_{K-1/2} - w_{K+1/2} = 0, \tag{56}$$

where the e subscript has now been dropped from "vertical velocity" in the s-coordinate. The obvious form of the temperature equation (21) is

$$\frac{\partial}{\partial t}(h_K T_K) + \nabla \cdot (\mathbf{u}_K h_K T_K) + (wT)_{K-1/2} - (wT)_{K+1/2}$$
$$= Q_{K-1/2} - Q_{K+1/2} + h_K D_K. \tag{57}$$

Summing these equations over all layers and horizontal points shows that, in the absence of sources and sinks, the heat content in finite difference form

$$\text{Heat Content} = \sum_{K=1}^{NZ} \langle h_K (T_K - T_B) \rangle \tag{58}$$

would be conserved, where angle brackets denote an area average. This requires that the divergence operator be conservative (which it is, except at the boundaries) and is independent of the values assumed for T at the layer interfaces. However,

(57) is not the form of the heat equation used; instead we choose to split the horizontal divergence term into three parts and to substitute from (56) for the layer divergence. This gives the form

$$\frac{\partial}{\partial t}(h_K T_K) - \frac{1}{2} T_K \frac{\partial h_K}{\partial t} + \frac{1}{2}\nabla\cdot(\mathbf{u}_K h_K T_K) + \frac{1}{2} h_K \mathbf{u}_K \cdot \nabla T_K$$
$$+ w_{K-1/2}(T_{K-1/2} - \tfrac{1}{2}T_K) - w_{K+1/2}(T_{K+1/2} - \tfrac{1}{2}T_K)$$
$$= Q_{K-1/2} - Q_{K+1/2} + h_K D_K. \tag{59}$$

It remains to specify the temperatures at the layer interfaces and this is done by considering which invariant to conserve in finite difference form. Consider the finite difference form of the temperature variance

$$\text{Temperature Variance} = \sum_{K=1}^{NZ} \langle h_K (T_K - T_B)^2 \rangle. \tag{60}$$

Its conservation is analyzed by multiplying (59) by T_K and summing. The two horizontal advection terms can then be written as a single divergence term which sums to zero, and it remains to ensure that the vertical advection terms sum to zero. The only choice that makes this possible is

$$T_{K-1/2} = \tfrac{1}{2}(T_{K-1} + T_K), \qquad T_{K+1/2} = \tfrac{1}{2}(T_K + T_{K+1}), \tag{61}$$

so that this is the form that conserves temperature variance. However, the finite difference form of the potential energy (28) is

$$\text{Potential Energy} = \sum_{K=1}^{NZ} \left\langle h_K b_K \left(\sum_{j=1}^{K-1} h_j + \frac{h_K}{2} \right) \right\rangle - \frac{1}{2} g \langle z_T^2 \rangle, \tag{62}$$

with z_T given by (53). Its conservation is analyzed by multiplying (57) by $-\alpha g z_K$ and adding $(P_K + \alpha g z_K T_B)$ times (56). Some algebra then shows that the w terms sum to zero if and only if the layer interface temperatures are given by (49). This is the form used in the model, which then conserves temperature variance (60) if and only if the layer depths are equal. It is shown in [1] that in sigma coordinates, if the hydrostatic equation is differenced locally, then only one of energy and temperature variance can be conserved. The finite difference form of the kinetic energy (26) is

$$\text{Kinetic Energy} = \sum_{K=1}^{NZ} \langle \tfrac{1}{2} h_K \mathbf{u}_K \cdot \mathbf{u}_K \rangle. \tag{63}$$

Its conservation is analyzed by considering the dot product of the finite difference form of the momentum equation with $\mathbf{u}_K$. Thus its conservation is assured by assuming layer interface velocities to be the simple averages given in (48) and to

employ an equation with similar advection properties to that for temperature (59). Thus the finite difference form of the momentum equation (20) is

$$\frac{\partial}{\partial t}(h_K \mathbf{u}_K) - \frac{1}{2}\mathbf{u}_K \frac{\partial h_K}{\partial t} + \frac{1}{2}\nabla \cdot (\mathbf{u}_K h_K \mathbf{u}_K) + \frac{1}{2} h_K \mathbf{u}_K \cdot \nabla \mathbf{u}_K$$
$$+ w_{K-1/2}(\mathbf{u}_{K-1/2} - \tfrac{1}{2}\mathbf{u}_K) - w_{K+1/2}(\mathbf{u}_{K+1/2} - \tfrac{1}{2}\mathbf{u}_K)$$
$$+ f\mathbf{k} \times h_K \mathbf{u}_K + \mathbf{PGF}_K = \boldsymbol{\tau}_{K-1/2} - \boldsymbol{\tau}_{K+1/2} + h_K \mathbf{F}_K, \tag{64}$$

where the pressure gradient force is given by (55).

The model finite difference equations are (56), (59), and (64) with the pressure gradient force, b_K and z_T defined by Eqs. (55), (52), and (53), respectively. The stability of these equations is discussed in Section 6b. Diagnostic quantities are given by (58), (60), (62), and (63) and equations for these quantities will be given in the next section when the forcing and vertical dissipation terms have been specified.

(f) *Unstratified Model*

The finite difference equations of the unstratified model are (56) and (64), where the pressure gradient force is given by the simplified form

$$\mathbf{PGF}_K = \frac{b\rho}{\rho_0} h_K \nabla \left(\sum_{K=1}^{NZ} h_K \right). \tag{65}$$

The unstratified model kinetic energy is still given by (63), and an available potential energy can be derived from (62) for this simpler model, and is given by

$$\text{Potential Energy} = \frac{b\rho}{2\rho_0} \left\langle \left(\sum_{K=1}^{NZ} h_K \right)^2 - \left(\sum_{K=1}^{NZ} h_K(t=0) \right)^2 \right\rangle. \tag{66}$$

Equation (59) can be thought of as an equation for a passive scalar in the unstratified model.

4. Vertical Coordinate, Forcing, and Vertical Mixing

(a) *Mixed Layer*

The upper layer of the model, $K=1$, is taken to represent the well-mixed layer at the ocean surface. The velocities and temperature are considered as constant in this layer so that T_1 is sea surface temperature (SST). The model has three possibilities to represent the physics of the mixed layer: (i) the depth of this mixed layer remains constant, i.e.,

$$h_1 = \text{const} \Rightarrow w_{1\,1/2} = \nabla \cdot (h_1 \mathbf{u}_1); \tag{67}$$

(ii) a true layer, with no entrainment or detrainment of fluid from the base of the layer, i.e., $w_{1\,1/2}=0$; (iii) the entrainment or detrainment at the base of the mixed layer is determined by an equation derived, for example, from a Kraus–Turner model [6]. This option is similar to the method described in [11]. The upper layer depth is then given by (56) with $K=1$.

(b) *Remaining Layers*

The vertical coordinate s over the remaining layers has been chosen to be like a sigma coordinate which divides the total depth of these layers into prescribed fractions. A sigma coordinate is most often used in atmospheric models with pressure as the vertical coordinate and divides the atmosphere into layers with prescribed fractions of the total model pressure difference, see [5]. With this vertical coordinate, the first step is to update the total depth of layers 2 through NZ. This is done by summing (56) over these layers to obtain

$$\frac{\partial}{\partial t}\left(\sum_{K=2}^{NZ} h_K\right)+\sum_{K=2}^{NZ}\nabla\cdot(h_K\mathbf{u}_K)+w_{1\,1/2}=0, \tag{68}$$

where $w_{1\,1/2}$ is given by (67) or mixed layer physics and w is zero at the base of the model. The total depth is divided into the separate layer depths by

$$h_K=\sigma_K\left(\sum_{K=2}^{NZ} h_K\right), \tag{69}$$

where σ_K, $K=2$, NZ is prescribed beforehand. The vector σ is such that

$$\left(\sum_{K=2}^{NZ}\sigma_K\right)=1, \qquad \sigma_1=\frac{\langle h_1\rangle}{\sum_{K=2}^{NZ}\langle h_K\rangle}, \tag{70}$$

and σ_1 has been defined as in (70) for convenience.

Now that the time derivatives of all the layer depths from 2 to NZ are known, repeated application of Eq. (56) with $K=2$, $NZ-1$ is used to calculate the remaining $w_{K+1/2}$'s diagnostically. Thus the entrainment or detrainment at the base of the mixed layer, $w_{1\,1/2}$, has to be predicted but the remaining w's governed by a sigma-type coordinate are calculated diagnostically. Now that all the w's are known, the velocities $\mathbf{u}_K$ and temperatures T_K, $K=1\cdots NZ$ can be updated using (64) and (59).

A fourth model option treats the total fluid depth using a sigma coordinate. In this case, the sums in the definition of the σ's, (69) and (70), start at $K=1$ rather than $K=2$. In this more usual case the total layer depth is first predicted by summing (56) over all the layers. Then all the w's are calculated diagnostically by repeated application of (56) with $K=1$, $NZ-1$. Finally all the velocities and temperatures are updated using (64) and (59).

(c) *Surface Forcing*

The surface stress $\tau_{1/2}$ and heat flux $Q_{1/2}$ in the model are assumed to affect directly only the upper mixed layer, $K=1$. They can be general prescribed functions of $\mathbf{x}$ and t or can depend upon the model variables in the upper layer. The forms used at present are simple and well known: $\tau_{1/2}$ is constant in space and time and

$$Q_{1/2}(\mathbf{x}, t) = \Theta(T_A - T_1), \tag{71}$$

where T_A is some prescribed "atmospheric" temperature, presently set to a constant; T_1 is the model SST; and Θ is a constant heat flux per degree centigrade.

(d) *Vertical Mixing*

The finite difference forms of vertical mixing in the model are approximations of the continuous forms

$$\tau = \frac{\nu_V}{h}\frac{\partial \mathbf{u}}{\partial s}, \qquad Q = \frac{\kappa_V}{h}\frac{\partial T}{\partial s}, \tag{72}$$

where ν_V and κ_V are the vertical eddy diffusivity and conductivity. The finite difference forms are

$$\tau_{K+1/2} = \mathrm{BINT}_{K+1/2}\frac{\mathbf{u}_K - \mathbf{u}_{K+1}}{\sigma_K + \sigma_{K+1}}, \qquad \tau_{NZ+1/2} = \mathrm{BINT}_{NZ+1/2}\frac{\mathbf{u}_{NZ}}{\sigma_{NZ}}, \tag{73}$$

$$Q_{K+1/2} = \mathrm{CINT}_{K+1/2}\frac{T_K - T_{K+1}}{\sigma_K + \sigma_{K+1}}, \qquad Q_{NZ+1/2} = \mathrm{CINT}_{NZ+1/2}\frac{T_{NZ} - T_B}{\sigma_{NZ}}. \tag{74}$$

The internal terms merely redistribute momentum and heat within the layers, but the bottom terms are sinks of these two quantities. The finite difference forms (73) and (74) are approximations to (72) because they have sigmas in the denominators rather than the actual depth between the midpoints of layers K and $K+1$, which is a function of $\mathbf{x}$ and t. The definition of sigma in (69) then gives the relations

$$(\mathrm{BINT}, \mathrm{CINT}) = 2(\nu_V, \kappa_V)\Big/\sum_{K=2}^{NZ}\langle h_K\rangle. \tag{75}$$

Equation (75) indicates that, if the depth of layers $2-NZ$ increases, then the values of BINT and CINT should be reduced to keep the same values of ν_V and κ_V. However, this is only true for the well-resolved vertical wavenumbers and, with only a few model layers, no vertical wavenumber is well resolved. In fact, the vertical friction and thermal damping act primarily on the shortest possible vertical wavelengths. A simple analysis shows that BINT and CINT should be proportional (not inversely proportional) to the depth of layers $2-NZ$ in order for the damping on the $2\Delta s$ wave to remain the same. These forms for vertical mixing give the

following forms for the budgets of total energy, heat content (HC) and temperature variance (TV):

$$\frac{\partial}{\partial t}(KE+PE)=\Big\langle \boldsymbol{\tau}_{1/2}\cdot\mathbf{u}_1-\sum_{K=1}^{NZ-1}\mathrm{BINT}_{K+1/2}\frac{(\mathbf{u}_K-\mathbf{u}_{K+1})^2}{(\sigma_K+\sigma_{K+1})}$$
$$-\mathrm{BINT}_{NZ+1/2}\frac{\mathbf{u}_{NZ}^2}{\sigma_{NZ}}+\alpha g Q_{1/2}\left(\frac{h_1}{2}-z_T\right)$$
$$+\frac{\alpha g}{2}\sum_{K=2}^{NZ}h_K\sum_{K=1}^{NZ-1}\mathrm{CINT}_{K+1/2}(T_K-T_{K+1})$$
$$+\alpha g\,\mathrm{CINT}_{NZ+1/2}(T_{NZ}-T_B)\frac{z_{NZ}}{\sigma_{NZ}}$$
$$+\sum_{K=1}^{NZ}h_K(\mathbf{u}_K\cdot\mathbf{F}_K-\alpha g z_K D_K)\Big\rangle, \tag{76}$$

$$\frac{\partial}{\partial t}(HC)=\left\langle Q_{1/2}-\mathrm{CINT}_{NZ+1/2}\frac{(T_{NZ}-T_B)}{\sigma_{NZ}}+\sum_{K=1}^{NZ}h_K D_K\right\rangle, \tag{77}$$

$$\frac{\partial}{\partial t}(TV)=\Big\langle T_1 Q_{1/2}-\sum_{K=1}^{NZ-1}\mathrm{CINT}_{K+1/2}\frac{(T_K-T_{K+1})^2}{(\sigma_K+\sigma_{K+1})}$$
$$-\mathrm{CINT}_{NZ+1/2}\frac{T_{NZ}}{\sigma_{NZ}}(T_{NZ}-T_B)$$
$$+\sum_{K=1}^{NZ-1}\frac{1}{2}w_{K+1/2}(T_K-T_{K+1})^2\frac{(\sigma_K-\sigma_{K+1})}{(\sigma_K+\sigma_{K+1})}+\sum_{K=1}^{NZ}h_K T_K D_K\Big\rangle. \tag{78}$$

Equation (76) shows that internal friction and friction and thermal damping at the model base act to reduce the energy in the active ocean layer, whereas internal thermal damping acts to increase it by mixing warmer water downward. Equation (77) shows that the total heat content is only changed by the surface heat flux, thermal damping at the base of the model, and horizontal damping, which is usually small. Equation (78) shows that temperature variance is reduced by thermal damping and has the spurious finite difference term when the layer depths are not equal; see the discussion in Section 2(e). The forms (76)–(78) also assume no contributions from horizontal finite differences; see the discussions in Sections 3(b) and 5.

5. Horizontal Smoothing and Friction

(a) *Shapiro Filter*

The horizontal smoothing in the model is the filter devised by Shapiro [12]. In one dimension, the filter of order n is defined by

$$\bar{f}_i^n=f_i-F^{n/2}(f_i), \tag{79}$$

where

$$F(f_i) = \tfrac{1}{4}(2f_i - f_{i+1} - f_{i-1}). \tag{80}$$

Here n must be an even integer and is twice the order of the filter as originally defined in [12]. We use this definition of n because $n/2$ repetitions of the finite difference operation F, which reaches to points $i \pm n/2$, is a finite difference approximation of $\partial^n/\partial x^n$ which is second-order accurate in Δx. Thus

$$F^{n/2}(f_i) \approx (-1)^{n/2}\gamma \frac{\partial^n f}{\partial x^n}, \tag{81}$$

where

$$\gamma = (\Delta x/2)^n. \tag{82}$$

Thus the filter of order n is like the nth differential operator with a coefficient that depends upon the grid spacing. The coefficient of one quarter in (80) is chosen such that, whatever the value of n, the coefficient of the $2\Delta x$ wave in f_i is set to zero in $\bar{f}_i^n$ by the filter. This filter suppresses nonlinear computational stability by eliminating the $2\Delta x$ wave. By eliminating it completely during each application, the filter does not have to be applied each timestep for the computation to remain stable. The less often the filter is applied, the less viscous is the solution. The amount of smoothing is also very dependent upon the order n of the filter chosen. The higher the value of n, the fewer waves with shorter wavelengths are affected by the filter, such that when $n = 16$ all waves longer than $4\Delta x$ are virtually unaffected by the filter.

In a bounded domain, a boundary condition for the filtering must be imposed. In the model there is a choice between two possibilities: a conservative scheme and no change at the boundary. These are accomplished by

$$\text{Conservative,} \qquad F(f_0) = \tfrac{1}{4}(f_0 - f_1), \tag{83}$$

$$\text{No change at boundary,} \qquad F(f_0) = 0. \tag{84}$$

The conservative scheme means that the sums of f_i and $\bar{f}_i^n$ over all i points are the same and the no change at the boundary scheme means that f_i and $\bar{f}_i^n$ have the same boundary values. We note that use of either scheme means that the coefficient of the $2\Delta x$ wave is not set exactly to zero at the boundary. Also, if the grid is stretched as described in Section 3(a), then the conservative scheme does not conserve line integral quantities unless the variable f is modified by the varying line segments Δx before the filtering is done (see Section 9).

The model also has the option to use the Shapiro filter with reduced order near the boundaries. With this option, the order of the filter at the point adjacent to the boundary is 2, at the next point the order is 4, etc., until the full order n is achieved at the $(n/2)$th gridpoint from the boundary. This idea was first used in [9]. The main reason to use this option is that the stratified model rapidly becomes unstable at the boundaries if uniform filters of order 8 or more are used. This is not true of

the unstratified model which remains stable using uniform filters of order 8, 16, or 32. However, the stratified model is much more sensitive and is always unstable with uniform filters of order 8 or more. Thus the stratified model uses the reduced order filter. This can also be justified physically by the argument that friction and mixing are greatest at ocean boundaries and so should be in the model where the boundary motions are well resolved. The reduced order filter also has the advantage that only the usual frictional boundary conditions are applied and no arbitrary, higher order boundary conditions are needed. The reduced order filter uses (83) or (84) only once at the boundary, which means that the "conservative" scheme is not conservative even when the grid is uniform. The reduced order filter can be made truly conservative (see Section 9). The coefficient of the $2\Delta x$ wave is not set to zero near the boundaries, and this might mean that filtering has to be done more frequently than in a model where this coefficient is set to zero, i.e., using a uniform filter in a doubly periodic domain (see Section 9). The model filters $h\mathbf{u}$, hT, and h first in x and then in y after a given number of Lorenz N-cycles (see Section 6). This means that the order of the reduced filter is asymmetric in x and y near the boundaries, as in [11], whereas the reduced order filter in [9] is symmetric in x and y.

(b) *Boundary Conditions*

The inviscid boundary conditions are the usual ones of zero normal velocity at solid boundaries and no boundary conditions on temperature. The model has a choice of three different velocity boundary conditions and two different temperature frictional boundary conditions. They are

$$\mathrm{MBC} = \begin{cases} 1. \text{ No slip at all boundaries.} \\ 2. \text{ No slip at E, W and slip at N, S boundaries.} \\ 3. \text{ Slip at all boundaries.} \end{cases} \tag{85}$$

$$\mathrm{MTC} = \begin{cases} 1. \text{ Temperature specified at N, S boundaries and zero heat flux at E, W boundaries.} \\ 2. \text{ Zero heat flux at all boundaries.} \end{cases} \tag{86}$$

These boundary conditions are implemented by using the appropriate form of the Shapiro filter, i.e., no change at boundary if $\mathbf{u}$ or T have specified boundary values, and conservative if $\mathbf{u}$ or T are not specified. For options $\mathrm{MBC} = 2$ and $\mathrm{MTC} = 1$, this requires using the different filter options in the x and y directions. h is also filtered with constant order in the unstratified model and with reduced order in the stratified model (see Section 9). In the code, the filtering is done after the boundary conditions have been applied.

(c) *Laplacian Friction*

In order to compare the effects of the Shapiro filter with other frictional forms used in numerical models, we have implemented Laplacian and biharmonic friction

forms. For simplicity, these forms were only tested with a uniform horizontal grid and then compared to runs using the filter on the same grid.

For Laplacian friction, the forms in Eqs. (20) and (21) are

$$\mathbf{F} = \nu_H \nabla^2 \mathbf{u}, \qquad D = \kappa_H \nabla^2 T, \tag{87}$$

with no friction in the continuity or h equation (22). The boundary conditions are no slip and zero normal derivative of temperature at all boundaries. The Laplacian operator is approximated in finite difference form by

$$\frac{\partial^2 f}{\partial x_i^2} \approx \frac{(f_{i+1} + f_{i-1} - 2f_i)}{(\Delta x)^2}, \tag{88}$$

which is second-order accurate in Δx. The boundary form for temperature is

$$\frac{\partial^2 f}{\partial x_0^2} \approx \frac{2(f_1 - f_0)}{(\Delta x)^2}. \tag{89}$$

A boundary form for velocity is not needed because of the no slip boundary condition.

(d) *Biharmonic Friction*

The biharmonic friction forms used in (20) and (21) are

$$\mathbf{F} = -\tilde{\nu}_H \nabla^4 \mathbf{u}, \qquad D = -\tilde{\kappa}_H \nabla^4 T, \tag{90}$$

again with no friction in the h equation (22). Extra boundary conditions have to be specified with these forms. We have chosen to implement no slip and zero second normal derivative of velocity and zero first and third normal derivative of temperature. The higher order boundary conditions seem the most logical to use given the usual frictional boundary conditions. These different boundary conditions on velocity and temperature mean they require different finite difference forms next to the boundaries. The finite difference forms are again only specified for use with a uniform horizontal grid and are second-order accurate in Δx. The interior form is

$$\frac{\partial^4 f}{\partial x_i^4} \approx \frac{(f_{i+2} + f_{i-2} - 4f_{i+1} - 4f_{i-1} + 6f_i)}{(\Delta x)^4}. \tag{91}$$

The next to the boundary form for velocity is

$$\frac{\partial^4 f}{\partial x_1^4} \approx \frac{(f_3 - 4f_2 + 5f_1 - 2f_0)}{(\Delta x)^4}. \tag{92}$$

A boundary form for velocity is again not needed because of the no slip boundary condition. The forms for temperature next to and on the boundaries are

$$\frac{\partial^4 f}{\partial x_1^4} \approx \frac{(f_3 - 4f_2 + 7f_1 - 4f_0)}{(\Delta x)^4}, \tag{93}$$

$$\frac{\partial^4 f}{\partial x_0^4} \approx \frac{2(f_2 - 4f_1 + 3f_0)}{(\Delta x)^4}. \tag{94}$$

(e) *Consistency and Convergence*

We have given the accuracy of the horizontal and vertical differencing and horizontal smoothing and friction schemes. It is straightforward to demonstrate the consistency of the finite difference equations except for the Shapiro filter where the coefficient γ depends upon Δx, see Eq. (82). Thus the coefficient of the nth derivative in the Shapiro filter changes if the horizontal resolution is changed, and in fact tends to zero as $\Delta x \to 0$. Thus the model formally becomes inviscid as $\Delta x \to 0$ and it is inconsistent to apply the viscous boundary conditions. This difficulty can be overcome by defining γ in (82) to be the maximum of a constant γ^* and $(\Delta x/2)^n$. The finite difference equations are now formally consistent with the partial differential equations and, as $\Delta x \to 0$ when $\gamma = \gamma^*$, the numerical solution is convergent.

In practice the filter is used with γ given by (82). Thus, if the horizontal resolution is doubled, then γ is much reduced and the solution is less viscous. However, in geophysical fluid numerical modeling, if the option to double the horizontal resolution exists, then the coefficient of Laplacian or biharmonic friction chosen would be reduced by factors proportional to $(\Delta x)^2$ and $(\Delta x)^4$, respectively. The reason is that these subgrid scale mixing parameterizations are needed to maintain numerical stability by suppressing nonlinear computational instability and to provide sinks at the smallest resolvable scales of the model. In fact, the biharmonic friction was first used because it separates more distinctly the dissipation scale from the energy-containing scale than does Laplacian friction. Thus the Shapiro filter and Laplacian and biharmonic frictions are used in a similar way in practical computations.

6. Time Method and Stability

(a) *Time Differencing*

The model uses the N-cycle time differencing scheme of Lorenz [7], with N equal to four. To solve the equation

$$\frac{\partial \mathbf{u}}{\partial t} = f(\mathbf{u}, t), \tag{95}$$

where $\mathbf{u}$ is a vector and f is a matrix, the scheme may be described as follows. Let the timestep be δt and define $\Delta t = N\,\delta t$. The timesteps are counted by an index n, which is zero initially, and the vector $\mathbf{u}$ is set to its initial value. The scheme is

$$1. \quad m = n \bmod N, \tag{96}$$

$$2. \quad a_n = \frac{-m}{\Delta t}, \qquad b_n = \frac{\Delta t}{(N-m)}, \tag{97}$$

$$3. \quad \mathbf{v}^n = b_n[a_n \mathbf{v}^{n-1} + f(\mathbf{u}^n, t^n)], \tag{98}$$

$$4. \quad \mathbf{u}^{n+1} = \mathbf{u}^n + \mathbf{v}^n, \tag{99}$$

$$5. \quad n = n + 1. \tag{100}$$

With N set to 4, the scheme is fourth-order accurate in Δt if f is linear, but only second-order accurate in Δt if f is nonlinear. The scheme also has the property that at any intermediate step, m less than N, the solution is correct to first order in Δt. These convergence properties of our time scheme are derived in detail in [7], see Eq. (18).

(b) *Linear Stability*

In this subsection we examine the computational stability of Eq. (95), where f is considered to be linear and a purely advective operator. In this situation let $\lambda_j = i\lambda_A$ be the timestep Δt times the jth eigenvalue of f. Then the growth rate, G_j, of the mode with eigenvalue λ_j for the Lorenz scheme is

$$G_j = \sum_{n=0}^{N} \frac{\lambda_j^n}{n!}. \tag{101}$$

Computational stability requires that all growth rates are such that $|G_j| \leqslant 1$. With $N = 4$, Eq. (101) gives

$$|G_j|^2 = 1 - \frac{\lambda_A^6}{72} + \frac{\lambda_A^8}{(24)^2}, \tag{102}$$

which shows that the scheme is stable and damping if $\lambda_A < \sqrt{8}$. When $\lambda_A \ll 1$, (101) can be approximated by

$$G_j \approx e^{i\lambda_A} - \frac{(i\lambda_A)^{N+1}}{(N+1)!}. \tag{103}$$

For N even,

$$|G_j|^2 \approx 1 - 2(-1)^{N/2} \frac{\lambda_A^{N+2}}{(N+1)!}, \tag{104}$$

which shows that the Lorenz scheme is damping if N is a multiple of 4, but need not be so when N is an odd multiple of 2.

We now consider the timestep restriction due to an advective term of the form cu_x. The maximum eigenvalue of the fourth-order centered scheme (44) is $1.37/\Delta x$, so that the timestep restriction is

$$\lambda_A = 1.37c\frac{\Delta t}{\Delta x} < \sqrt{8}. \tag{105}$$

With the 4-cycle scheme $\Delta t = 4\,\delta t$ and for a two dimensional equation, the timestep restriction from (105) becomes

$$\delta t < 0.5 \Big/ c\left(\frac{1}{\Delta x} + \frac{1}{\Delta y}\right). \tag{106}$$

Here δt is in seconds, Δx and Δy are in m and an appropriate speed c is 3 m/s because it is larger than any wave or advective speed attained in model runs. This advective restriction on the timestep is much more severe than that due to vertical mixing in the form described in Section 4(d). This analysis is based on work in [2, 4].

7. Unstratified Model Experiments

In this section we describe a series of experiments using the 2-layer unstratified version of the model that were run in order to compare the effects of various horizontal smoothing techniques. The experiments use either constant easterly wind stress or constant southerly wind stress of 0.5 dyne/cm^2 and the model is integrated to 2000 days. A no slip condition is applied at the boundaries. Other details of the model setup and parameter values for these experiments are given in Table I. The

TABLE I

Unstratified Model Parameter Values

Domain	$30° \times 30° \times 200$ m
Resolution	$60 \times 60 \times 2$
Horizontal	Uniform of $\frac{1}{2}°$
Vertical	Constant 40 m, initial 160 m
$b\rho/\rho_0 =$	0.019 m/s^2
BINT =	1.5×10^{-5} m/s
$\tau^x =$	-0.5 or 0 dynes/cm^2
$\tau^y =$	0 or 0.5 dynes/cm^2
Lorenz N-cycle, $N = 4$	
$\delta t =$	$\frac{1}{32}$ days or 45 mins
$\Delta t =$	$\frac{1}{8}$ days or 3 h
Uniform filter order 8 and 16 applied every $\frac{1}{2}$ day	
Uniform filter order 32 applied every 0.04 days	
Reduced filter order 16 applied every $\frac{1}{2}$ day	
Laplacian friction	$\nu_H = 4 \times 10^3$ m^2/s
Biharmonic friction	$\tilde{\nu}_H = 4 \times 10^{12}$ m^4/s

model has a constant depth mixed layer of 40 m and a variable depth layer below that is uniformly 160 m at $t = 0$. The density difference between these two layers and the resting ocean below is set at 2×10^{-3} g/cm^3. The value of vertical friction is equivalent to a $\nu_V = 12$ cm^2/s acting over the 160 m layer. The time integration scheme used is the Lorenz 4-cycle scheme.

The horizontal smoothers used are the uniform Shapiro filter of order 8, 16, and 32, the reduced filter of order 16, Laplacian and biharmonic frictions. All experiments are run as close to the stability boundary as possible. Applying the uniform filter every 0.5 days for order 16 is the largest number of complete Lorenz 4-cycles that maintains stability during the spin-up phase of the experiments. The filter was also applied every 0.5 days when the order was 8. When the order was 32, however, a smaller timestep had to be used and the filter had to be applied after every Lorenz 4-cycle in order to maintain stability. The Laplacian and biharmonic

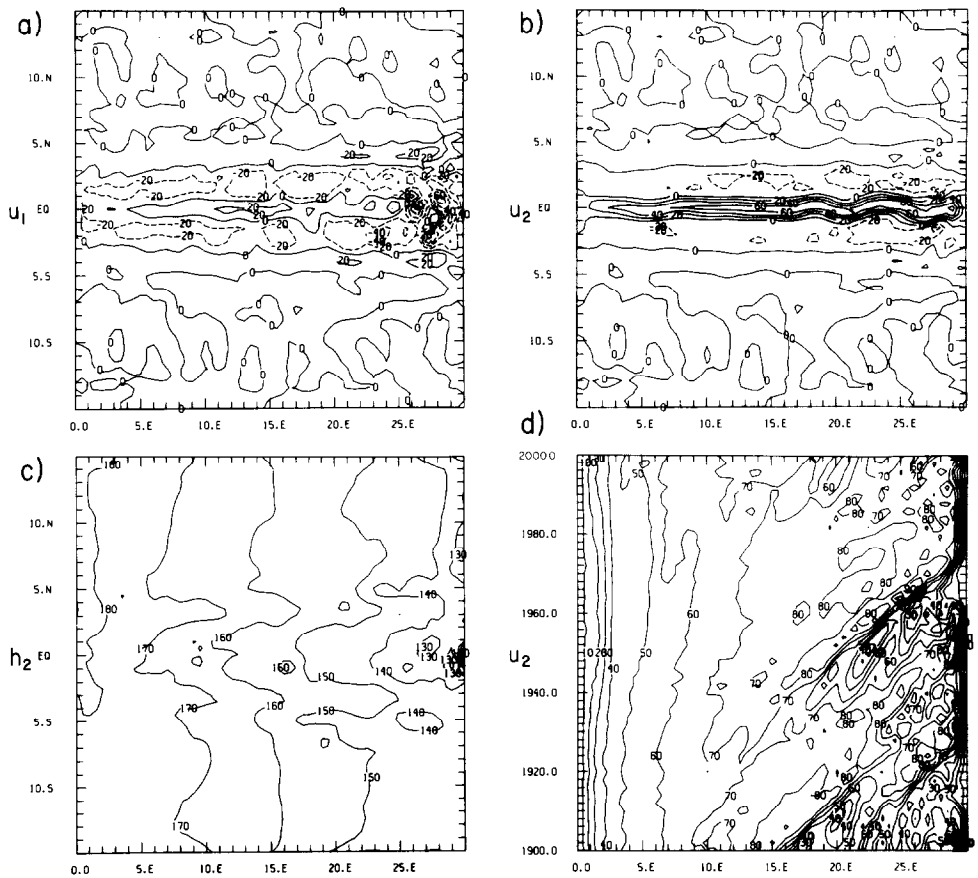

FIG. 2. Unstratified model equilibrium response to constant east wind stress of 0.5 dynes/cm^2, using order 16 uniform filter. (a) u in upper layer; (b) u in lower layer; (c) h in second layer, and (d) u along the equator in lower layer against time for last 100 days of spin up.

friction values of 4×10^3 m^2/s and 4×10^{12} m^4/s are also the minimum values required to maintain stability during the spin-up phase. If the frictions were reduced to 3×10^3 and 3×10^{12}, then either the east or the south wind case blew up during spin-up from rest.

First we describe the different equilibrium states in the two cases using easterly or southerly wind stress. The zonal velocities in the two layers and the depth of the second layer at 2000 days in the east wind case using the uniform Shapiro filter of order 16 are shown in Fig. 2. In the upper layer there is mostly westward flow with some return flow in the countercurrents. Most of the water is returned to the east by the undercurrent in layer 2. At the equator, the second layer is much deeper in the west and much shallower in the east than the average depth of 160 m. The undercurrent in this case is slightly unstable and has meanders in the eastern half of the domain. These meanders propagate eastwards as shown by Fig. 2d, which is a plot of u_2 along the equator against time for the last 100 days of the experiment. This instability for east winds only occurs when using the uniform filter of order 32 or 16, and the equilibrium state is truly time independent in the remaining cases. The fact that these cases have more damping than the uniform order 32 and 16 filter cases is also borne out by the equilibrium values of KE and PE, which are given in Table II. There is not a large difference in the PE values since the largest contribution comes from the basin wide slope in the depth of the second layer.

TABLE II

Unstratified Model Experiments: Values of KE/10^{13} and PE/10^{13} at 2000 Days and Percentage Losses during 100 Days Spindown.

Case		Easterly wind stress		Southerly wind stress	
Uniform filter order 32	KE	2.75	−75.8%	4.38	−79.4%
	PE	1.89	−73.4%	2.42	−49.7%
Uniform filter order 16	KE	2.32	−73.5%	4.24	−78.2%
	PE	1.85	−77.0%	2.63	−55.3%
Uniform filter order 8	KE	2.04	−73.5%	3.90	−87.2%
	PE	1.79	−75.3%	2.17	−57.2%
Reduced filter order 16	KE	1.97	−73.1%	3.93	−85.2%
	PE	1.92	−76.0%	2.19	−58.8%
Biharmonic friction	KE	1.50	−83.3%	3.27	−92.7%
	PE	1.71	−76.5%	2.05	−62.0%
Laplacian friction	KE	1.02	−90.9%	2.16	−97.1%
	PE	1.67	−84.3%	1.93	−65.3%
Uniform filter order 16, no VF	KE	2.32	−40.1%	4.24	−49.6%
	PE	1.85	−64.6%	2.63	−38.0%
Laplacian friction, no VF	KE	1.02	−85.4%	2.16	−96.6%
	PE	1.67	−81.6%	1.93	−63.2%

There are large differences in the values of KE, however, with the Laplacian friction value being about half the filter values.

There is a much stronger instability in the south wind case. Figure 3 shows the zonal velocities and lower layer depth at 2000 days in this case again when the order 16 uniform filter is used. The waves now propagate westward, as is shown in Fig. 3d, which is again a plot of u_2 against time for the last 100 days of the experiment. For south winds there are stronger local depth variation and velocities than for east winds, so that the final PE and KE are larger in this case. The instability is much stronger for south winds and occurs with all the horizontal smoothers. It is rather weak in the Laplacian friction case, however, which again has an equilibrium KE value about half the filter values. All the equilibrium values of KE and PE for south winds are also given in Table II.

A series of spindown experiments was also run. The forcing is switched off and the model is run for an additional 100 days, and then the percentage reductions in

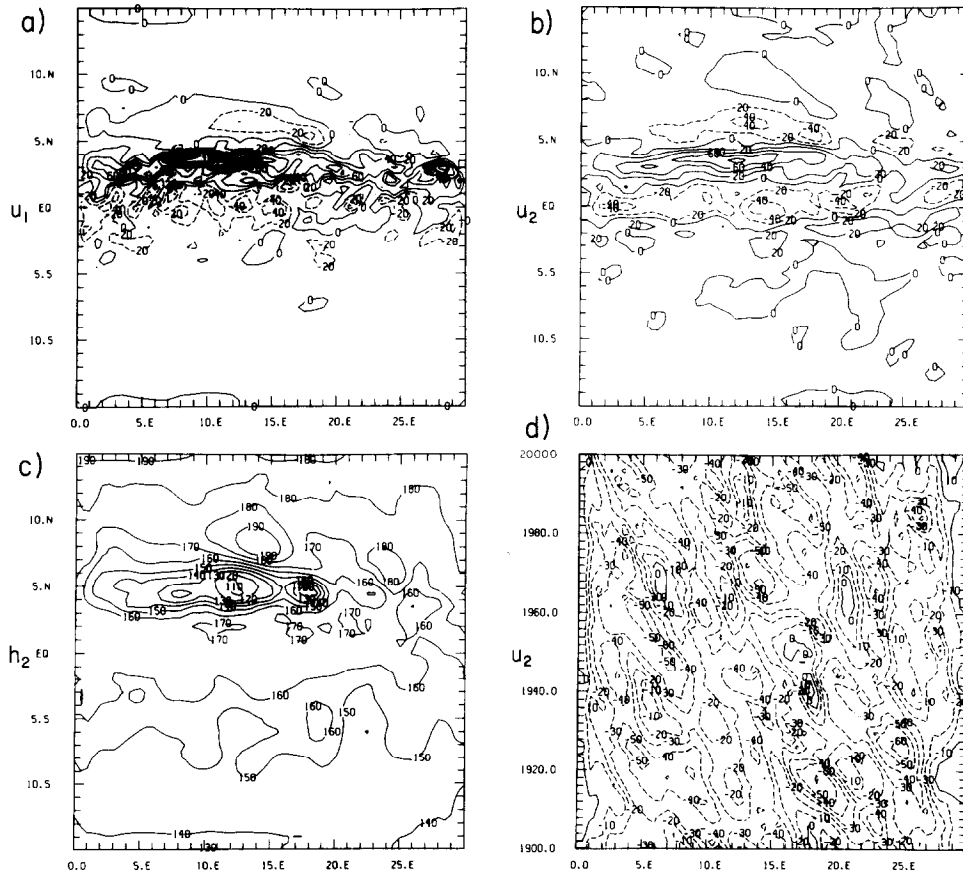

FIG. 3. Same as Fig. 2 except for constant south wind stress of 0.5 dynes/cm^2.

both kinetic and available potential energy are calculated. The KE and PE would eventually go to zero if the model were allowed to spindown completely. The evolution of KE and PE over the 100 day spindown experiments for the order 16 uniform filter are shown in Fig. 4. The KE drops much more steeply initially for the south wind case as the instability source is switched off and the local velocities decrease. The KE decrease is much more uniform in time in the east wind case and the percentage loss of KE is smaller than in the south wind case. For PE, however, the opposite occurs and the initial decrease is much steeper in the east wind case. This is also a result of the forcing being switched off, which results in the very fast adjustment of the lower layer depth away from its uniform east–west slope along the equator in the equilibrium state. This adjustment is accomplished by equatorial waves, mainly by the Kelvin wave, in the first 12 days. The PE decrease in the

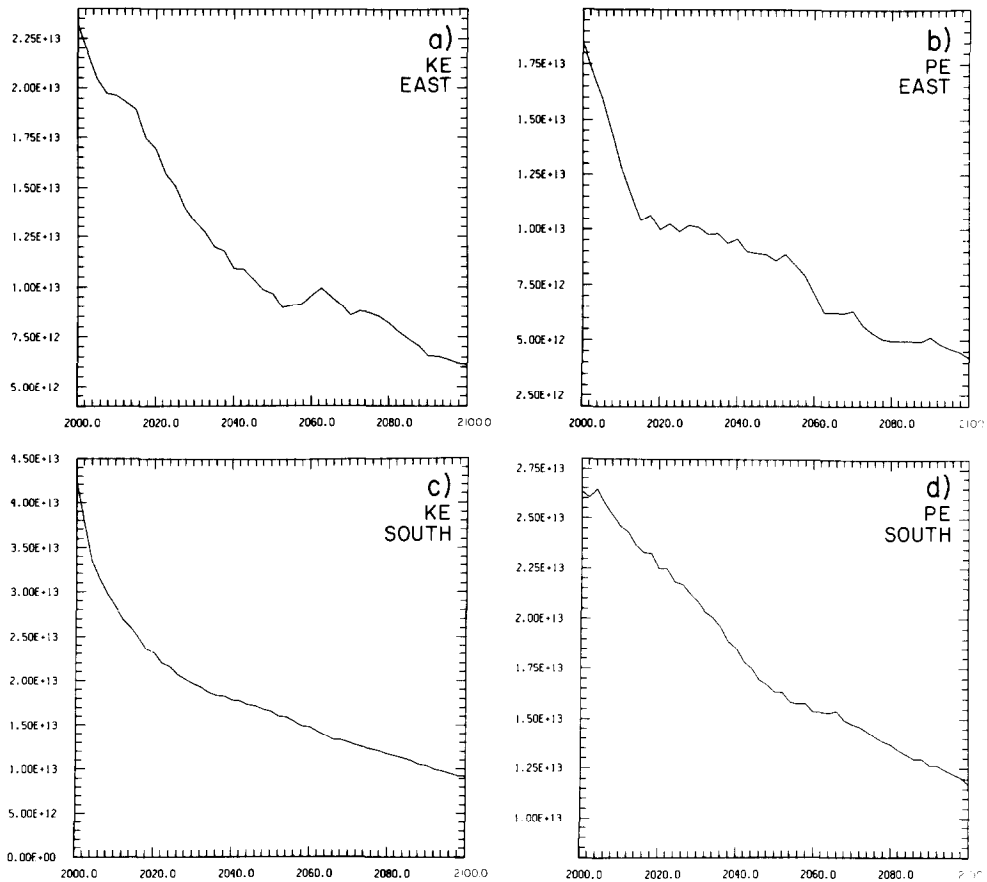

FIG. 4. Plots of kinetic and potential energy against time for 100 days of spin down experiments using order 16 uniform filter in the unstratified model: (a) KE; (b) PE from east wind case; (c) KE and (d) PE from the south wind case.

south wind case is much more uniform with time and the percentage lost in 100 days in this case is much smaller than in the east wind case.

These differences between the east and south wind spindown cases are similar when using any of the other horizontal smoothers, but the percentage reductions in energy vary considerably between horizontal smoothers. The cases are listed in Table II starting with the order 32 uniform filter, which loses least energy down to Laplacian friction, which loses most. It is not accidental that this order would be the same if the criterion were the amount of energy in the equilibrium state. For the order 16 uniform filter and Laplacian friction, the spindown experiments were repeated with no vertical friction. With Laplacian friction the percentage reductions are not much smaller than when vertical friction is present, which shows that the horizontal damping is the major energy sink. For the order 16 uniform filter, however, the percentage reductions are much smaller, which shows that vertical friction is a very significant energy sink. This is also known to be true in the equatorial oceans and was the major criterion by which we judged the various horizontal smoothers. Another criterion in favor of the high-order filter cases is their much higher overall values of KE and PE in the equilibrium state. Table II also shows that there is little advantage in the order 32 uniform filter over the order 16 uniform filter in terms of energy spindown, whereas the computation cost is many times larger because of the smaller timestep, more computation per filtering, and filtering much more often. The filtering is a significant fraction of the total computation in the order 32 case, whereas the fraction is much smaller in the order 16 cases, when it is about the same as using Laplacian or biharmonic friction. We prefer the order 16 uniform filter to the order 8 uniform and order 16 reduced filters because of the higher equilibrium energy values and the smaller percentage reductions during spindown. Thus we conclude that, for the unstratified model, the order 16 uniform filter is the best choice of a weak horizontal smoother that is not excessive in computational cost.

8. Stratified Model Experiments

In this section we describe a series of experiments using the 5-layer stratified version of the model. The model forcing and configuration is the same as that described in Section 7 except that the lower layer is divided into four equal layers using the σ coordinate, each of which is 40 m deep initially. The model setup and parameters are given in Table III which shows that the vertical eddy conductivity is an order of magnitude smaller than the eddy diffusivity and is equivalent to $\kappa_V = 1.2\ \mathrm{cm}^2/\mathrm{s}$ acting over the 160 m layers. The heat flux into the ocean is relative to a constant atmospheric temperature of 30°C at a rate of $30\ \mathrm{W/m}^2\,^\circ\mathrm{C}$. No slip and zero heat flux conditions apply at the boundaries. The time step for the stratified model is slightly smaller than that for the unstratified version. We compare runs using the Shapiro filter of order 16 and 8 both of which are reduced to order 2 at the boundaries (necessary to retain stability), and Laplacian and bihar-

TABLE III

Stratified Model Parameter Values

Domain	$30° \times 30° \times 200$ m
Resolution	$60 \times 60 \times 5$
Horizontal	Uniform of $\frac{1}{2}°$
Vertical	Constant 40 m, initial 4×40 m
$\alpha =$	$2.55 \times 10^{-4}\,°C^{-1}$
$g =$	9.8 m/s^2
BINT =	1.5×10^{-5} m/s
CINT =	1.5×10^{-6} m/s
$\tau^x =$	-0.5 or 0 dynes/cm^2
$\tau^y =$	0 or 0.5 dynes/cm^2
$\Theta =$	30 W/m^2 °C
$T_A =$	30°C
Lorenz N-cycle, $N = 4$	
$\delta t =$	0.025 days
$\Delta t =$	0.1 days
Reduced filter order 8 and 16 applied every 0.4 days	
Laplacian Friction	$\nu_H = 4 \times 10^3$ m^2/s
	$\kappa_H = 10^3$ m^2/s
Biharmonic Friction	$\tilde{\nu}_H = 4 \times 10^{12}$ m^4/s
	$\tilde{\kappa}_H = 10^{12}$ m^4/s

monic friction. We again use $\nu_H = 4 \times 10^3$ m^2/s or $\tilde{\nu}_H = 4 \times 10^{12}$ m^4/s and a smaller horizontal thermal diffusion of 10^3 m^2/s or 10^{12} m^4/s. The cases were run to equilibrium, 10 and 5 years for the easterly and southerly wind cases, respectively. The equilibrium values of KE, PE, and heat content (HC), given by Eqs. (63), (62), and (58), are listed in Table IV. In the stratified model, PE is not an available potential energy, as in the unstratified model, and is thus much larger than the KE at equilibrium in these experiments. The KE, PE, and HC are all defined such that they would eventually go to zero if the model were allowed to spindown completely.

The equilibrium state with constant easterly wind stress of 0.5 dyne/cm^2 using the reduced filter of order 16 is shown in Fig. 5. It shows the zonal velocities in the upper two layers, the free surface elevation z_T and the sea surface temperature, and can be compared to Fig. 2 from the unstratified model. For east winds, the surface velocity is again mostly westward, most of which is returned to the east by the equatorial undercurrent. This current is strongest in the second layer and weakest in the fifth layer. The surface elevation slopes upwards to the west with a difference of 25 cm at the equator across the 30° of longitude. The corresponding depth of layers two to five increases to the west, but the changes along the equator are reduced from those in the unstratified model. Most of the longitudinal changes in surface elevation are caused by temperature, not depth, variations as there is a difference of 8°C in sea surface temperature across the basin at the equator. The model was integrated for 10 years in this case because of the long adjustment time for temperature (due to small κ_V) and the fact that the final state had a weak

TABLE IV

Stratified Model Experiments: Values of $KE/10^{12}$, $PE/10^{15}$, and $HC/10^{3}$ at 10 Years (East) and 5 Years (South) and Percentage Losses during 100 Days Spindown

Case		Easterly wind stress		Southerly wind stress	
Reduced filter order 16	KE	10.0	−57.9%	14.0	−78.9%
	PE	4.22	−5.1%	4.10	−3.6%
	HC	2.19	−5.6%	2.13	−5.3%
Reduced filter order 8	KE	9.9	−58.3%	10.1	−83.0%
	PE	4.21	−5.2%	4.12	−3.6%
	HC	2.19	−5.6%	2.13	−5.4%
Biharmonic friction	KE	8.9	−50.4%	7.0	−84.3%
	PE	4.31	−5.0%	4.14	−3.7%
	HC	2.19	−5.7%	2.14	−5.4%
Laplacian friction	KE	4.6	−65.7%	3.3	−81.5%
	PE	4.36	−5.0%	4.13	−3.7%
	HC	2.21	−5.7%	2.13	−5.4%
Reduced filter order 16, no VF	KE	10.0	+51.7%	14.0	−38.5%
	PE	4.22	−0.4%	4.10	−0.1%
	HC	2.19	+0.2%	2.13	+0.2%
Laplacian friction, no VF	KE	4.6	+4.7%	3.3	−67.7%
	PE	4.36	−0.3%	4.13	−0.2%
	HC	2.21	+0.1%	2.13	+0.1%

instability and was not quite time independent. For east winds, this situation occurred when using any of the four horizontal smoothers.

In contrast, all four cases with southerly winds stress of 0.5 dyne/cm^2 go to a genuine steady state. It is shown in Fig. 6 using the order 16 reduced filter, and can be compared to Fig. 3 from the unstratified model. In both model versions the zonal currents are much more barotropic than in the east wind case and the maximum zonal velocities are at about 3°N. There is a corresponding minimum in surface elevation z_T at this latitude, just as there was a minimum in layer depth in the unstratified model. There is relatively little gradient in sea surface temperature from the equator to 5°N so that the layer depth variations have a significant effect on surface elevation in this region. This is in contrast to the situation along the equator in the east wind case.

The cases in Table IV have been listed in order of the amount of KE in the equilibrium state. For the east wind case, the values for the reduced filter of order 16 and 8 are almost the same because most of the small scale velocity variance is near the boundaries where there is no difference between these filters. In the south wind case some of the small scale velocity variance is away from the boundaries and the order 16 reduced filter has significantly more KE. As for the unstratified model, the

Laplacian friction cases have the least KE: it is less than 50% and 25% of the order 16 reduced filter KE in the east and south wind cases, respectively. There are only small differences in the values of PE and almost no difference in the HC values using the different horizontal smoothers. This indicates that the layer depths and temperatures have large horizontal scales and their equilibrium values are dictated mostly by the value of the vertical heat diffusion. The PE and HC values change slowly with time and take a long time to reach their equilibrium values.

Spindown experiments were also run with the stratified model and the percentage losses in KE, PE, and HC over a period of 100 days are listed in Table IV. The evolution of KE, PE, and HC for the east wind case with the order 16 reduced filter are shown in Fig. 7. It shows that initially there is a conversion of PE to KE which remains above its equilibrium value for 25 days before decreasing to 42% of its equilibrium value after 100 days. In contrast, PE and HC decrease slowly and

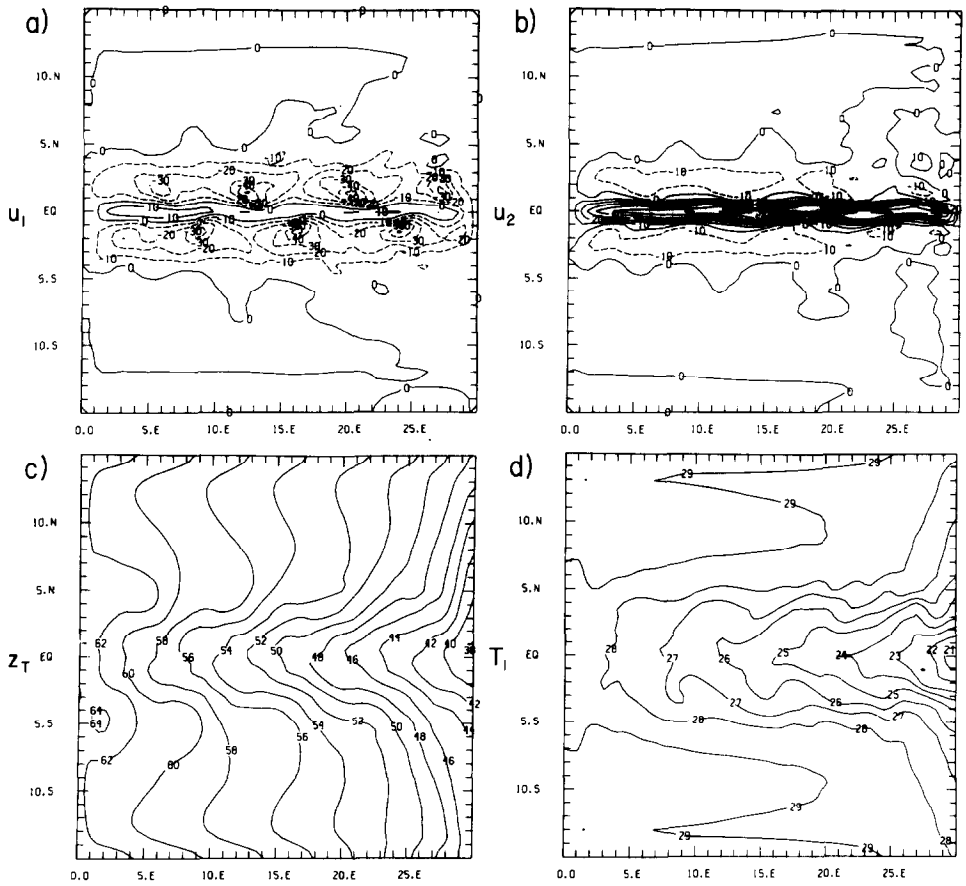

FIG. 5. Stratified model equilibrium response to constant east wind stress of 0.5 dynes/cm^2, using order 16 reduced filter: (a) u in upper layer; (b) u in second layer; (c) free surface elevation z_T; and (d) T in upper layer.

almost linearly over the entire 100 days. This long decay time is determined by, and is inversely proportional to, the vertical heat diffusion κ_V. In a comparison experiment starting from the same equilibrium state, but with κ_V increased by a factor of ten, PE and HC decreased by 45.0% and 53.5%, respectively, compared to decreases of 5.1% and 5.6% in the standard case. Also shown in Fig. 7(d) is the evolution of KE over 100 days when there is no vertical friction. In this case KE increases by 70% of its equilibrium value in the first 15 days and remains at over 150% of its equilibrium value for the entire 100 days. In the same time PE only decreases by 0.4% but, because of its much larger equilibrium value compared to KE, the total energy of the flow does decrease over the 100 days. This shows that the major sinks of KE, PE, and HC in the stratified model are vertical friction and heat diffusion as is desired on physical grounds.

The evolution of KE, PE, and HC for the south wind case with the order 16

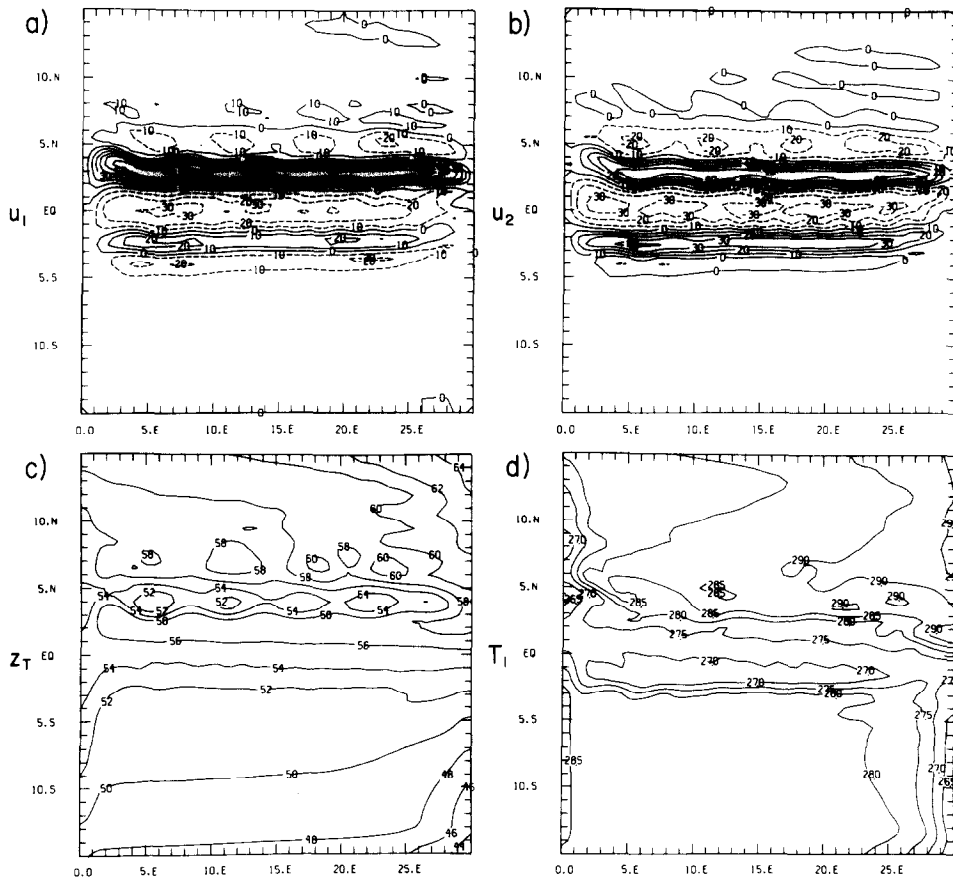

FIG. 6. Same as Fig. 5 except for constant south wind stress of 0.5 dynes/cm^2.

reduced filter are shown in Fig. 8. In this case KE falls uniformly and smoothly to only 21% of its equilibrium value after 100 days, and again PE and HC decrease slowly and almost linearly over the entire 100 days. Figure 8(d) shows the evolution of KE over 100 days when there is no vertical friction. There is a small initial increase in KE, but after 100 days it has decreased to 62% of its equilibrium value which again shows that vertical friction is the major sink of KE. PE and HC are essentially unchanged over 100 days in the no vertical friction case, which shows that their major sink is vertical thermal diffusion. With Laplacian friction this dominance of vertical over horizontal damping processes is considerably reduced; see Table IV.

Table IV also shows that there is relatively little difference in percentage reduc-

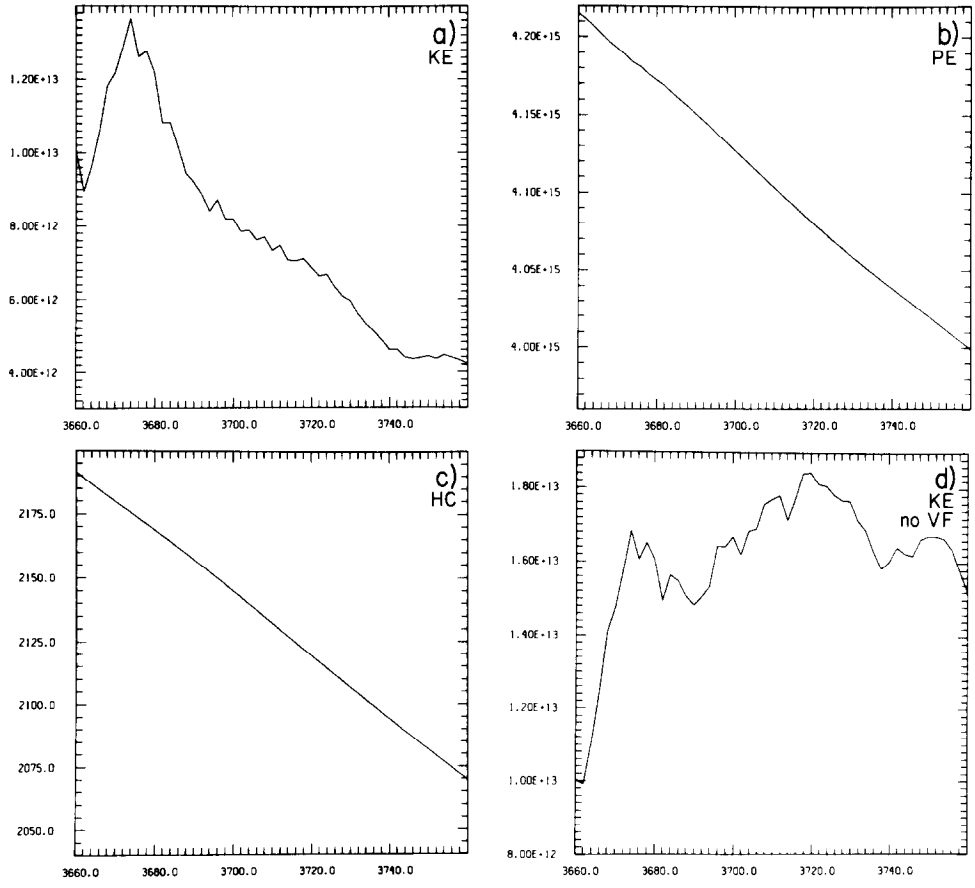

FIG. 7. Plots of kinetic and potential energy and heat content against time for 100 days of spin down experiment using order 16 reduced filter in the stratified model with east wind stress: (a) KE; (b) PE; (c) HC; and (d) KE from a similar experiment with no vertical friction.

tions between the horizontal smoothers when vertical friction is present. This is in contrast to the unstratified model where the differences are quite large. This much more comparable energy loss in the stratified model is due to the necessity of using the reduced order filter so that the smoothing near the boundaries is now quite large. There are two reasons why we still prefer the filter over Laplacian and biharmonic friction in the stratified model. The first is that the flow is much less damped as indicated by the equilibrium values of KE in Table IV. The second is that the differences in percentage reductions between the filter and the other frictions in spindown experiments increases when more points than the 60×60 used here are employed. This will certainly be the case in most model applications. Also with a stretched grid the high dissipation region of the filter will be smaller than when the grid is uniform, which again reduces the dissipation effects of the filter compared to the other frictions. Thus we conclude that, for the stratified model, the order 16 reduced filter is the best choice of a weak horizontal smoother.

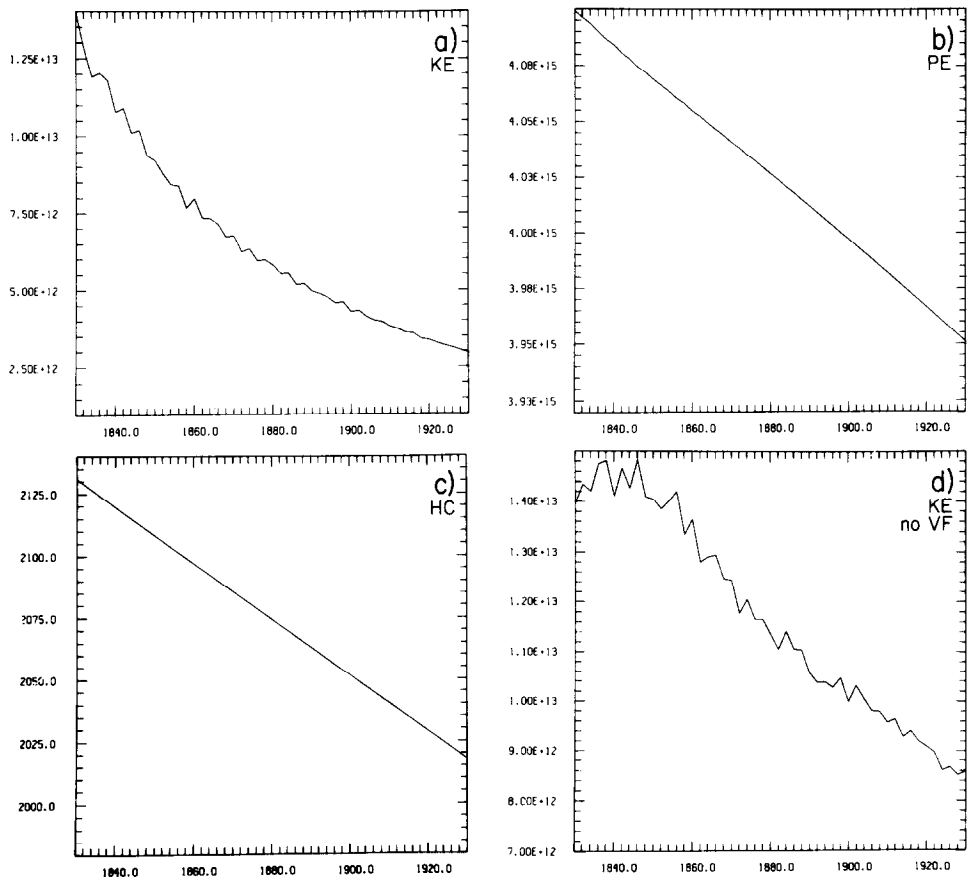

FIG. 8. Same as Fig. 7 except with south wind stress.

9. Choice of Filter

Since the horizontal average of the height field is time independent, a conservative filter should be applied to h. However, in our work with both versions of the model, we have found that a conservative filter is worse at suppressing the $2\Delta x$ wave near the boundaries than a nonconservative one, so that the conservative filter has to be applied more frequently to suppress nonlinear computational instability. For example, if the order 16 uniform filter is used in the unstratified model under the conditions given in Table I with the conservative (CON) filter (83) on h and the no change at boundary (NCAB) filter (84) on $h\mathbf{u}$, then experiments with east and south winds both fail. The experiments listed in Table II for these conditions in fact use the NCAB filter on both $h\mathbf{u}$ and h, i.e., the correct BC on $\mathbf{u}$, but the incorrect BC on h. Thus the model has errors in h due to this as well as the nonconservation of the horizontal differencing scheme described in Section 3(b). At the end of these experiments at day 2000, the error in the average depth of the 160 m second layer is 61 and 33 cm in the east and south wind cases, respectively. These values are given in Table V which lists the depth error in cm for several of the experiments described in Sections 7 and 8, and for some experiments described below. Our philosophy is to accept these depth errors of 0.4% and 0.2% after 2000 days for the following reasons. The greater numerical stability of the NCAB filter means that filtering can be done less frequently so that the ratio of horizontal to vertical damping in the model is minimized. The model is only intended to be run for several years, so that depth errors in the unstratified version are likely to always be less than 1%, which we find acceptable. We note here that conserving h would require modifying the horizontal differencing scheme near the boundaries and modifying the variables by the varying line segments Δx before filtering when the grid is stretched. Laplacian and biharmonic friction are not applied to h, but depth errors do occur due to the horizontal differencing near the boundaries. The errors are very small for Laplacian friction because the flows are much less energetic, and

TABLE V

Depth Error in cm of the 160 m Layer after 2000 Days (Unstratified Model) or 5 Years (Stratified Model): Order 16 Filter Applied Every 4 Lorenz 4-cycles with NCAB Filter on $h\mathbf{u}$.

Model	Grid	No. of points	Filter	BC on h, hT	East winds	South winds
Unstratified	Uniform	60×60	Uniform	NCAB	61	33
Stratified	Uniform	60×60	Reduced	CON	219	124
Unstratified	Uniform	60×60	Reduced	CON	306	162
Unstratified	Uniform	100×100	Reduced	CON	84	30
Unstratified	Stretched	60×60	Reduced	CON	21	86
Stratified	Stretched	60×60	Reduced	CON	120	—

slightly larger for the somewhat more energetic flows using biharmonic friction. The order 8 and 32 uniform filter experiments listed in Table II also use the NCAB filter (84) on both $h\mathbf{u}$ and h, and this is the form of the filter we recommend for the unstratified model.

The same questions arise for the reduced filter which has to be used in the stratified model and the answers are similar. The reduced filter can be made truly conservative, but we have found this to be more numerically unstable than other forms of the reduced filter. For example, if the order 16 reduced filter is used in the stratified model under the conditions given in Table III with a truly conservative filter on h and hT, and the NCAB filter on $h\mathbf{u}$, then the experiment with south winds fails. With east winds, the experiment runs to 5 years but the final fields contain a considerable amount of $2\Delta x$ noise. The experiments listed in Table IV for these conditions in fact use the NCAB filter (84) on $h\mathbf{u}$ and the conservative (CON) filter (83) on h and hT. However, as described in Section 5(a), the CON filter is not conservative when the reduced filter is used. The depth errors in the 160 m layer at 5 years in these experiments are 219 and 124 cm in the east and south wind cases, respectively, see Table V. These depth errors using the order 16 reduced filter are considerably larger than those for the unstratified model using the order 16 uniform filter, but less than the errors in the unstratified model using the order 16 reduced filter. These errors are 306 and 162 cm for the east and south wind cases, respectively, see Table V.

These depth errors with the reduced filter are quite large but are considerably reduced in most model applications when more than 60×60 points are used and the grid is stretched. First, we have run the unstratified model with a uniform grid of 100×100 instead of 60×60 points using the order 16 reduced filter. The depth errors at 2000 days are 84 and 30 cm (Table V) compared to 306 and 162 cm in the 60×60 case. Second, we have used the stretched grid employed in [2, 3]. This has $\alpha = 0.35$, $\beta = 0.037$ at the equator, $\alpha = 0.25$, $\beta = 0.03$ at the east and west boundaries, and $\alpha = 0.17$, $\beta = 0.02$ at the north and south boundaries. We have not modified the variables by the line segments Δx before filtering. In the unstratified model with 60×60 points using the order 16 reduced filter, this reduces the depth errors at 2000 days to 21 and 86 cm in the east and south wind cases, respectively. Third, this same stretched grid in the stratified model using the order 16 reduced filter reduces the depth error at 5 years from 219 to 120 cm in the east wind case (Table V). In this configuration, the south wind case failed, as it did using several other boundary condition forms of the order 16 reduced filter. These depth errors of 0.5% after 2000 days in the unstratified model and 0.75% after 5 years in the stratified model are much more acceptable given that the model will only be run for several years. We have run some experiments with the stratified model using the NCAB reduced filter on h and hT. Compared to experiments using the CON reduced filter on h and hT, the depth errors at 5 years are sometimes larger and sometimes smaller. However, with the stretched grid and using east winds, the CON filter on h and hT case is stable (Table V), whereas the NCAB filter on h and hT case failed. Thus, we conclude that the NCAB filter on h and hT is slightly less

stable than the CON filter on h and hT. We have also run experiments using the CON filter on $h\mathbf{u}$, but have found no advantage over the NCAB filter which is the correct boundary condition on $\mathbf{u}$. The order 8 and 16 reduced filter cases listed in Table IV use the NCAB filter (84) on $h\mathbf{u}$ and the CON filter (83) on h and hT, and this is the form of the filter we recommend for the stratified model.

10. Conclusions

We have described a reduced gravity, primitive equation model of the upper equatorial ocean. There are two versions of the model: unstratified and stratified. The model has a well-mixed layer at the surface, which is of constant depth in all experiments described here, and an ocean layer below, which can be divided into several numerical layers by means of a sigma coordinate. This concentrates the model resolution in the equatorial thermocline and undercurrent where the vertical shears are largest. The reduced gravity approximation means that the deep ocean is at rest and has constant density or temperature. The model is forced by surface wind stress and heating that act over the mixed layer. The vertical damping has the form of an interfacial drag and thermal diffusion. The numerical grid can be stretched in the horizontal and the finite differencing is fourth-order accurate in the horizontal and second-order accurate in the vertical. The time stepping method used is the N-cycle scheme of Lorenz [7].

We have chosen to use the order 16 Shapiro filter to suppress nonlinear computational instability for several reasons. In experiments with constant easterly or southerly wind stress, the filter consistently gave much higher equilibrium values of kinetic and available potential energy in the unstratified model and higher values of kinetic energy in the stratified model than the more familiar Laplacian and biharmonic frictions. In spindown experiments with the unstratified model, the filter loses much less energy than these frictions. In spindown experiments with the stratified model, the filter losses are comparable to those of the frictions. The reason is that the reduced order filter is needed in the stratified model to maintain numerical stability, and it has larger damping at the model boundaries. This is justified physically because friction and mixing are greatest at ocean boundaries, and so should be in the model where the boundary motions are well resolved when the grid is stretched. Finally, the filter requires less computation than Laplacian and biharmonic frictions when the grid is stretched. We have chosen to use the most stable boundary forms for the filter so that it can be applied as infrequently as possible. This minimizes the ratio of horizontal to vertical damping, which is what we want on physical grounds. Thus the filter uses incorrect boundary conditions on layer depths and temperatures. This introduces depth errors which have been shown to be less than 1% in experiments lasting several years. We find this error acceptable and have chosen not to make the horizontal differencing and filter truly conservative, which could be done but would require more computation.

REFERENCES

1. A. ARAKAWA AND M. J. SUAREZ, *Mon. Weather Rev.* **111**, 34 (1983).
2. M. A. CANE, Ph.D. thesis, Massachusetts Institute of Technology, 1975 (unpublished).
3. M. A. CANE, *J. Mar. Res.* **37**, 253 (1979).
4. M. ISRAELI AND D. GOTTLIEB, *Mon. Weather Rev.* **102**, 254 (1974).
5. A. KASAHARA, *Mon. Weather Rev.* **102**, 509 (1974).
6. E. B. KRAUS AND J. S. TURNER, *Tellus* **19**, 98 (1967).
7. E. N. LORENZ, *Mon. Weather Rev.* **99**, 644 (1971).
8. J. P. MCCREARY, *Philos. Trans. Roy. Soc. London A* **298**, 603 (1981).
9. S. MUDRICK, *J. Comput. Phys.* **20**, 33 (1976).
10. H. PETERS, M. C. GREGG, AND J. M. TOOLE, *J. Geophys. Res.* **93**, 1199 (1988).
11. P. S. SCHOPF AND M. A. CANE, *J. Phys. Oceanogr.* **13**, 917 (1983).
12. R. SHAPIRO, *Rev. Geophys. Space Phys.* **8**, 359 (1970).